

Article

Investigation of the Disintegration Characteristics of Neogene Mudstone at Different Burial Depths

Liang Peng ^{1,2}, Wenxue Du ^{1,2}, Ganggang Bai ^{1,2}, Lahuancairang ^{1,2}, Shixiang Yuan ^{1,2}, Juntao Li ³ and Peng Feng ^{3,4,*}¹ Qinghai Hydrogeology and Engineering Geology and Environgeology Survey Institute, Xining 810008, China² Hydrogeological and Geothermal Geological Key Laboratory of Qinghai Province, Xining 810008, China³ School of Architecture and Civil Engineering, Chengdu University, Chengdu 610106, China⁴ Key Laboratory of Hydraulic and Waterway Engineering of the Ministry of Education, Chongqing Jiaotong University, Chongqing 400074, China

* Correspondence: fengpengfx@163.com

Abstract: The complex structure of Neogene mudstone plays an important role in geological disasters. A close relationship exists between the mechanisms of mudstone landslides and the disintegration characteristics of rocks. Therefore, understanding the disintegration characteristics of Neogene mudstone at different depths is crucial for enhancing engineering safety and assessing landslide stability. This study employed Neogene mudstone from different depths to perform disintegration and plastic limit experiments and revealed the sliding mechanisms of landslides involving Neogene mudstone, providing theoretical support for mitigating mudstone geological disasters. Our results demonstrate that Neogene mudstone from different depths experiences varied stress conditions and pore water pressure due to geological actions, significantly affecting the disintegration characteristics. By ignoring the factors of the slip surface, the slake durability index of mudstone decreases with increasing burial depth, while the plasticity limit index tends to rise. The influence of groundwater, geo-stress, and pore structure on Neogene mudstones at different depths results in overall weak stability and disintegration. Landslide occurrences are likely connected to the mechanical properties of mudstones at the slip surface, where a low slake durability index and higher plasticity index make the mudstones prone to fracturing, breaking, and disintegrating once in contact with water.

Keywords: Neogene mudstone; disintegration characteristics; mudstone landslides; slake durability index



Citation: Peng, L.; Du, W.; Bai, G.; Lahuancairang; Yuan, S.; Li, J.; Feng, P. Investigation of the Disintegration Characteristics of Neogene Mudstone at Different Burial Depths. *Buildings* **2024**, *14*, 227. <https://doi.org/10.3390/buildings14010227>

Academic Editors: Yongqiang Zhou, Erdi Abi, Longlong Lv and Shaobo Chai

Received: 11 December 2023

Revised: 5 January 2024

Accepted: 8 January 2024

Published: 15 January 2024



Copyright: © 2024 by the authors. Licensee MDPI, Basel, Switzerland. This article is an open access article distributed under the terms and conditions of the Creative Commons Attribution (CC BY) license (<https://creativecommons.org/licenses/by/4.0/>).

1. Introduction

Neogene mudstone, frequently encountered in geotechnical engineering, has complex physical characteristics under the influence of multiple factors [1–3]. The plasticity and deformability of Neogene mudstones generally play a crucial role in geological disasters such as landslides, accompanying disintegration and weakening the strength of mudstone [4–7]. In addition, the burial depth also affects the disintegration of Neogene mudstone and the progression of landslides [8,9], with varying stress states, rock transformations, and geological effects at distinct levels [10,11]. Thus, a thorough investigation on the disintegration characteristics of Neogene mudstones at various burial depths is essential to better our comprehension of mudstone landslide mechanisms and the recognition of potential landslide hazards [12–15]. Researchers have investigated the disintegration characteristics of mudstone under varying conditions [16–19]. Luo et al. [20] conducted systematic research on the distribution and pore structure of mudstone, demonstrating a close relationship between the disintegration resistance of mudstone and its mineral composition. Huang et al. [21] performed disintegration tests on rock specimens, investigating their disintegration characteristics under dry–wet cycling conditions. Moreover, comparative studies on the disintegration characteristics of mudstone blocks in indoor environments, acidic conditions, and natural climates have been carried out [22,23]. In addition, Shen et al. [24]

explored the morphological and fractal features of mudstone during the disintegration process.

Indeed, after disintegration, mudstones form powdery soil material, with the plasticity index acting as a crucial metric reflecting the viscosity and plastic behavior of soil material [25,26]. Shimobe et al. [27] examined the correlation between undrained shear strength, liquidity index, and moisture content for both remolded and undisturbed soils. Through experimental studies, no significant patterns were shown to exist between the temperature change and variations in liquid and plastic limits [28]. During liquid limit tests on mixed clays containing structured crystals and amorphous kaolinite, Stanchi [29] and Jefferson [30] showed a minimal temperature influence on liquid and plastic limits. Swaify et al. [31] focused their analysis on the effects of liquid limit, degree of dispersion, moisture retention, and saturated cations on the geomaterial properties. Davidson et al. [32] compared remolded and undisturbed soils, attributing differences in liquid and plastic limits to sample packaging, soil moisture, and remolding degree. Stanchi et al. [33] conducted a regression analysis on the impact of organic matter and carbon molecules on the liquid and plastic limits of soil, affirming that the cohesion of particles with diameters smaller than 0.425 mm influences the liquid and plastic limit.

At the microstructural scale, Tang et al. [34] investigated the microstructural damage of rock specimens under uniaxial compression based on scanning electron microscopy experiments, offering detailed analyses of the evolution and development characteristics of microcracks. Howarth et al. [35] examined the shapes of microscopic particles using rock slice imagery, while Campbell et al. [36] conducted a quantitative investigation on rock microstructure utilizing optical microscopy. In addition, based on the experiment on Neogene mudstone, the microstructural characteristics and softening mechanisms of soft rocks under various conditions have been explored [37–39]. The mineral composition and geological features of mudstone showed a significant influence on its resistance to disintegration, with weathering, diagenesis, hydrothermal activities, and geological transportation serving as the key factors affecting the engineering properties of mudstones [40]. Zhang et al. [41] analyzed the microstructural alterations in mudstone after rainfall and discovered the loosening mineral microstructure of mudstone and increasing porosity, singling out illite as a crucial agent of internal binding expansion and structural impairment.

So far, studies on the disintegration characteristics of Neogene mudstones at varying depths and inquiries into their liquid and plastic limits after disintegration have been relatively scant. Based on laboratory experiments and statistical analyses, this manuscript investigates the disintegration characteristics of Neogene mudstones from different depths and their consequent effects on mudstone landslide stability. After introduction, Section 2 introduces the specimen preparation and methodology utilized in this manuscript. Then, Sections 3 and 4 show the effects of burial depth on the disintegration characteristics and slake durability index of Neogene mudstones at macro and micro levels, respectively. The discussion of the formation of the Zhangjiawan landslide is established in Section 5. Section 6 summarizes the whole study.

2. Specimen Preparation and Methodology

2.1. Specimen Preparation

The Neogene mudstones utilized in this study were captured from the Zhangjiawan landslide with a burial depth ranging from 13 m to 17 m, as shown in Figure 1. Initially, we inserted drill rods to the designated depth and employed flush mediums such as mud or air to evacuate borehole cuttings, cool the drill bit, and sustain the integrity of the borehole walls. Subsequently, the rock cores were collected at predetermined depth intervals, and the retrieved cores were extracted from the barrels, followed by cataloging and tagging. We conserved the integrity of the rock cores by placing them into appropriate protective casings for further investigation. Cylindrical specimens with dimensions of $\Phi 50 \text{ mm} \times 50 \text{ mm}$ and a mass of $240 \pm 20 \text{ g}$ were prepared for the disintegration experiments. Each specimen can be labeled as S-D, where S stands for Neogene mudstone, and D represents the depth of

mudstone. For instance, S-13 denotes Neogene mudstone at a depth of 13 m. Table 1 details the physical parameters of these samples.

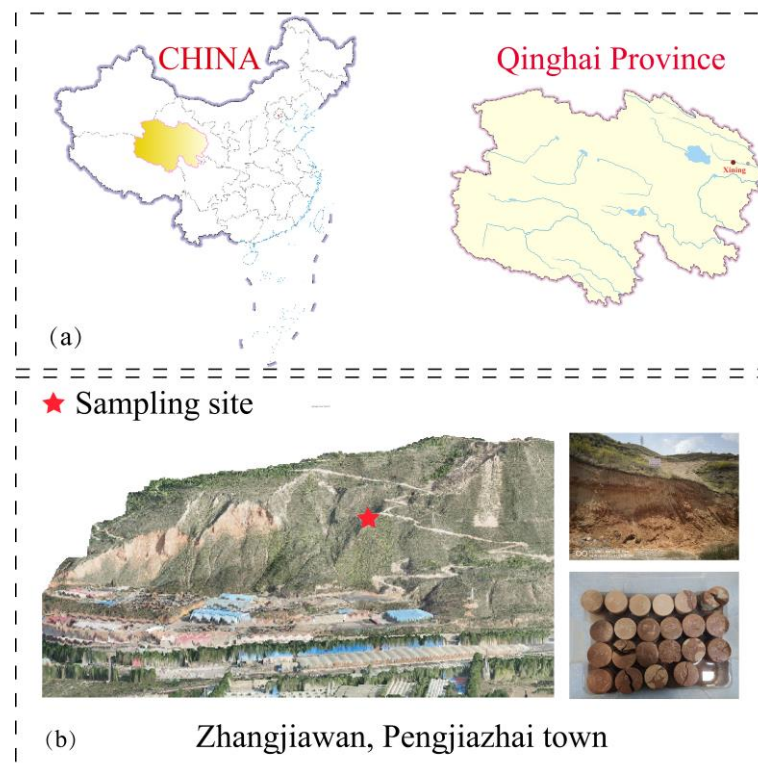


Figure 1. Preparation of Neogene mudstone specimens from Zhangjiawan landslide: (a) Qinghai province of China, (b) Sampling site.

Table 1. The geometrical parameters of Neogene mudstone at different depths.

Notation	Nature Weight (g)	Dry Weight (g)	High (cm)	Diameter (cm)	Density (g/cm ³)
S-13.0	248.68	221.70	5.420	5.037	2.30
S-13.2	240.54	216.62	5.163	5.056	2.32
S-13.4	226.29	202.95	4.895	5.044	2.31
S-13.7	230.44	204.60	5.129	5.011	2.28
S-14.0	229.79	203.87	5.039	5.015	2.31
S-14.3	230.52	205.59	5.076	5.041	2.28
S-14.6	231.09	205.88	5.106	5.043	2.27
S-16.7	227.25	192.09	5.123	5.010	2.25
S-17.0	251.95	222.88	5.532	5.045	2.28
S-17.3	242.89	215.29	5.298	5.046	2.29
S-17.5	229.69	205.28	4.985	5.047	2.30
S-18.0	223.75	199.27	5.114	5.000	2.23
S-19.0	231.71	206.62	5.136	4.916	2.38
S-19.3	244.08	219.46	5.318	5.043	2.30
S-19.6	237.85	213.14	5.140	5.045	2.31

An X-ray fluorescence spectrometer was employed to perform X-ray fluorescence spectroscopy on Neogene mudstone [42]. The principal chemical components of Neogene mudstone predominantly consist of SiO₂ and CaCO₃, accompanied by trace impurities, as illustrated in Figure 2.

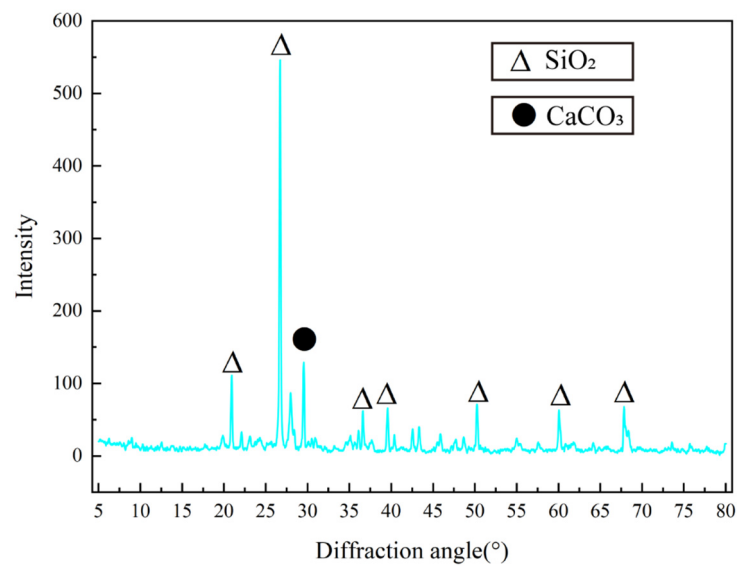


Figure 2. X-ray diffraction pattern of Neogene mudstone.

2.2. Methodology

2.2.1. Slake Durability Test

The slake durability index reflects the capability of a specimen to resist softening and disintegration, generally measured via slake durability tests. As shown in Figure 3d, the slake durability apparatus XYN-1 was adopted to determine the slake durability index [43,44]. The detailed experimental steps include: (1) Desiccating the samples at 100 °C for 24 h within an oven and then removing fragmented rocks and cooling the intact ones to ambient temperature. (2) Filling the trough with clear water, ensuring the water lies 20 mm beneath the rotary axis of the sieve drum. (3) After initiating the disintegration equipment, rotating at a velocity of 20 revolutions per minute for 10 min, and then drying the withdrawn sieve drum at 100 °C for another 24 h. (4) Weighing and recording the total mass of the rocks and the sieve drum. Following disintegration, sieving out and cataloging the residual fragments within the sieve drum, and thereafter reloading fragments with a particle size exceeding 2 mm back into the sieve drum. (5) Repeating the aforementioned steps until the sample exhibits consistent disintegration. The slake durability index can be calculated using Equation (1).

$$I_{dn} = \frac{m_n}{m_d} \times 100\% \quad (1)$$

where I_{dn} denotes the slake durability index after n standard cycles; m_n represents the initial dry mass of the sample; and m_d signifies the dry mass of the residual sample following the n standard cycle.

2.2.2. Plasticity Index Test

The plasticity index quantifies the difference between the liquid limit and the plastic limit of specimen under standard testing conditions, serving as a crucial parameter for characterizing the plastic deformation behavior of a specimen [45,46].

Determining the plasticity index of disintegrated mudstone can elucidate the extent and capability of its plastic deformation under stress. Plastic limit determination apparatus was employed to measure the liquid and plastic limits of the rock specimen, as shown in Figure 3e. The testing cone weighs 100 g and features an apex angle of 30 degrees. Initially, the dried specimens are passed through a 0.5 mm geotechnical sieve, the watered specimens are mixed thoroughly, and then they are sealed for over 18 h. Subsequently, the extracted samples are homogenized and placed into soil cups. The penetration depths of the samples are controlled below 5 mm, around 10 mm, and within 20 ± 0.2 mm to measure the plastic limit, intermediate value, and liquid limit, respectively. Once the penetration

depth is achieved, the test point is repositioned for a new measurement immediately, ensuring that the test points are at least 1 cm apart with an error margin of 0.5 mm. The average penetration depth is calculated at that point, suitable samples meeting the aforementioned penetration depth requirements are extracted, and then the moisture content is determined. Finally, based on the aforementioned value, the plasticity index of the specimen can be acquired in Equation (2).

$$P_I = L_L - P_L \quad (2)$$

where L_L and P_L represent the liquid limit and the plastic limit of the specimen; P_I represents the value of the plasticity index.

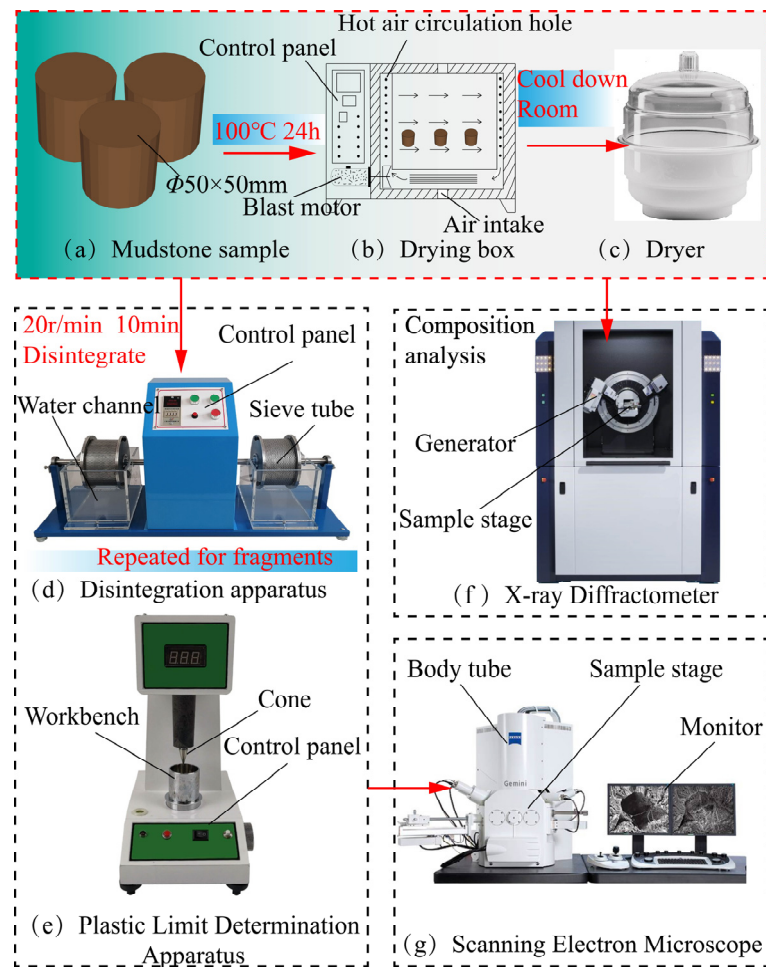


Figure 3. Experimental apparatus and experimental process for Neogene mudstone: (a) mudstone specimen, (b) drying box, (c) dryer, (d) disintegration apparatus, (e) plastic limit determination apparatus, (f) X-ray diffractometer, and (g) scanning electron microscope.

2.2.3. Scanning Electron Microscope System

The scanning electron microscope (SEM) system utilized in this study primarily consists of a vacuum system, an electron beam system, and an imaging system, as shown in Figure 3g. The electron beam system releases high-energy incident electrons that impact the surface of the material, directing a focused ultrafine beam onto the micro-observational surface and detecting the secondary electrons and backscattered electron signals induced by the electron beam system. Subsequently, signal processing enables the micro-observational surface of the specimen to be imaged [47,48]. This study employs SEM to perform the micro-scale scanning of Neogene mudstone, reaching a magnification of up to 10^6 times, offering an acceleration electric field for the projected electrons of up to 3×10^4 volts, and covering an effective scanning area of 10^{-2} mm for the specimens.

3. Results

3.1. Effects of Burial Depth on the Slake Durability Index of Neogene Mudstones

Figure 4 illustrates the slake durability index distribution of Neogene mudstone across various depths, with a noticeably higher value for depths ranging from 13 to 13.4 m; details are outlined in Table 2. Nevertheless, the slake durability index shows the lowest value at depths of 13.7 to 14 m. Overall, the slake durability index of Neogene mudstone trends downward with increasing depth. As the burial depth of mudstone escalates, groundwater leads to the absorption expansion and dissolution of Neogene mudstone. Simultaneously, Neogene mudstone experiences increasing permeation pressure and geo-stress, resulting in the alteration of its pore structure and promoting internal dissolution and fracturing, which in turn affects the slake durability index. The region between 13.7- and 14-m depth served as the sampling location for the landslide slip zone, which will undergo further discussion in Section 5.

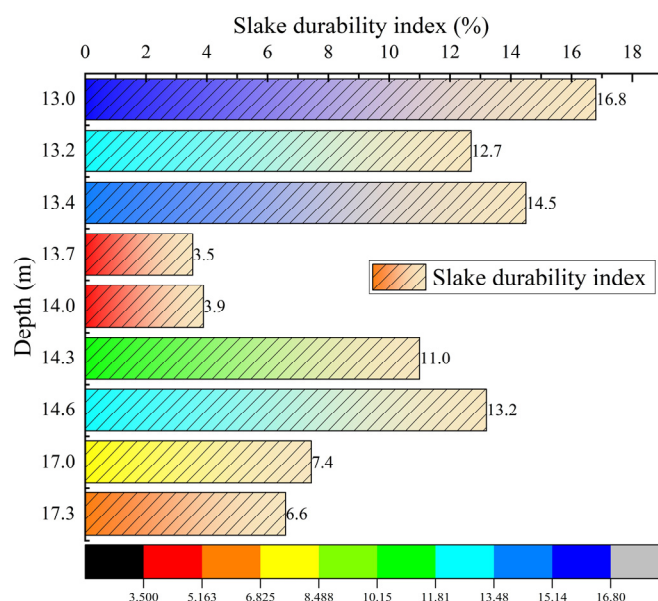


Figure 4. Slake durability index of Neogene mudstone under different depths; different color represents different value of the Slake durability index.

Table 2. The slake durability index of Neogene mudstones at different depths.

Notation	Sampling Site (m)	Slake Durability Index (%)
S-13.0	13.0–13.2	16.8
S-13.2	13.2–13.4	12.7
S-13.4	13.4–13.7	14.5
S-13.7	13.7–14.0	3.54
S-14.0	14.0–14.3	3.89
S-14.3	14.3–14.6	11.0
S-14.6	14.6–14.9	13.2
S-17.0	17.0–17.3	7.44
S-17.3	17.3–17.5	6.59

3.2. Effects of Burial Depth on the Plasticity Index of Neogene Mudstones

Figures 5 and 6 illustrate the liquid limits and plastic limits of Neogene mudstone at varied depths, showing notably lower values at depths ranging from 13 to 13.4 m, with the peaking value being between 13.7 and 14 m. In general, the higher liquid limits and plastic limits of Neogene mudstone can be characterized via the greater depth; details are shown in Table 3.

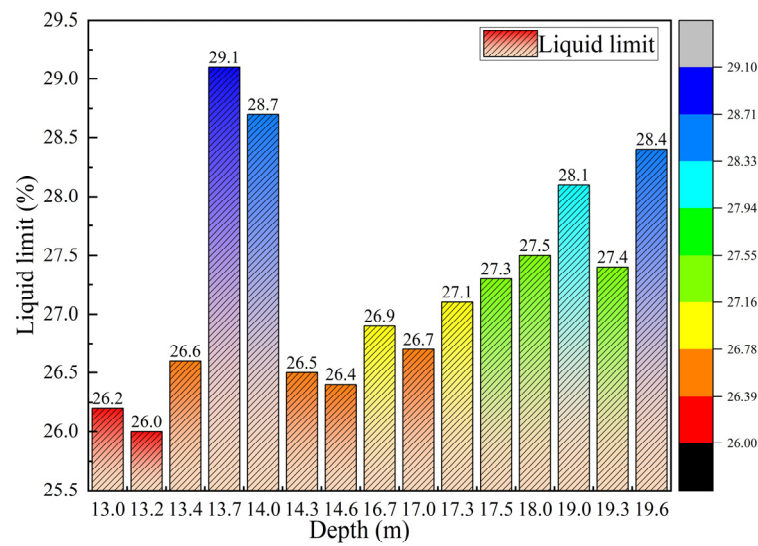


Figure 5. Effects of depth on the liquid limit of Neogene mudstone; different color represents different value of the liquid limit.

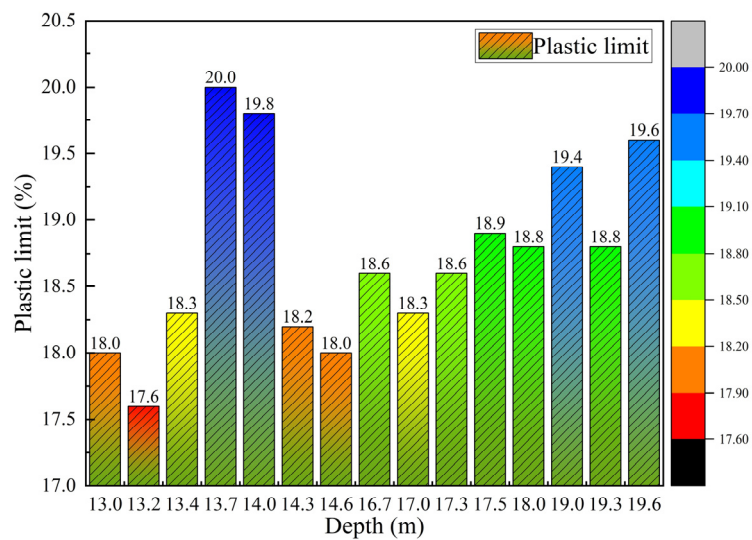


Figure 6. Effects of depth on the plastic limit of Neogene mudstone; different color represents different value of the plastic limit.

Table 3. The moisture content, liquid limit, plastic limit, and plasticity index of Neogene mudstone with different depths.

Notation	Moisture Content (%)	Liquid Limit (%)	Plastic Limit (%)	Plasticity Index (%)
S-13.0	3.4	29.1	20.0	9.1
S-13.2	0.9	26.1	17.8	8.3
S-13.4	3.2	26.7	19.2	7.5
S-13.7	2.8	26.3	17.4	8.9
S-14.0	1.2	27.9	19.8	8.1
S-14.3	3.6	25.4	18.1	7.3
S-14.6	2.1	24.9	17.9	7.0
S-16.7	1.1	26.5	18.7	7.8
S-17.0	1.6	26.9	19.3	7.6
S-17.3	2.5	25.8	17.6	8.2
S-17.5	3.9	25.7	17.8	7.9

Table 3. Cont.

Notation	Moisture Content (%)	Liquid Limit (%)	Plastic Limit (%)	Plasticity Index (%)
S-18.0	3.2	26.5	19.0	7.5
S-19.0	1.3	27.2	19.1	8.1
S-19.3	3.6	26.6	18.9	7.7
S-19.6	3.0	26.5	18.5	8.0

Figure 7 details the distribution of the plasticity index of Neogene mudstone at different depths, revealing a lower value from 13 to 13.4 m, and the highest index value was recorded between 13.7 and 14 m. Collectively, the plasticity index of Neogene mudstone shows an increasing trend with depth. Such results may be explicated by the diverse particle composition and structure at different mudstone depths, affecting the frictional interactions, bond strength, and deformation characteristics of Neogene mudstone, consequently impacting the plasticity index. As a matter of fact, elevated groundwater pressure and geo-stress at various depths can alter the pore structures of Neogene mudstone, leading to a higher water content in deeper strata, and thus also elevating the plasticity index.

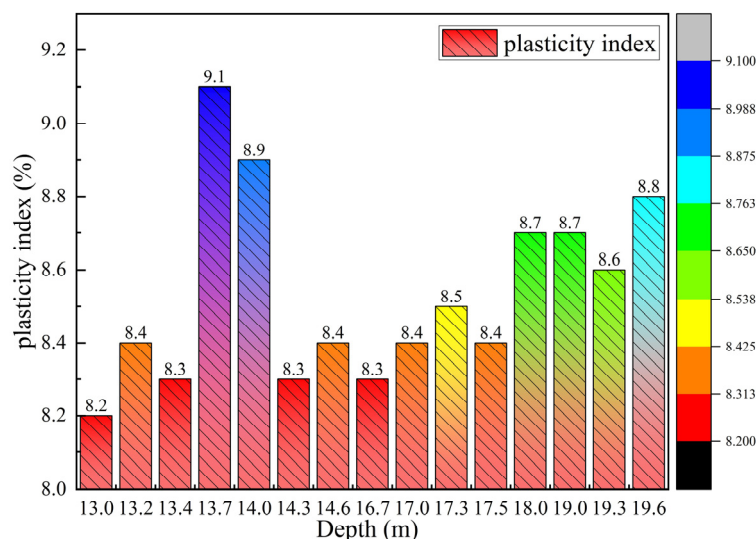


Figure 7. Effects of depth on the plasticity index of Neogene mudstone; different color represents different value of the plasticity index.

4. Microstructure Analysis

Figure 8 presents the SEM images of a typical Neogene mudstone sample after disintegration, revealing its microstructural characteristics. It can be observed that there is a rich content of hydrated clay minerals surrounding non-clay particles, creating a densely and unevenly agglomerated structure. The interior of these clay aggregates showcases a heterogeneous distribution of pores with significant size disparities. Large pores and a developed fractures segment fragment the cluster structure into several smaller sub-aggregates. Additionally, the clay minerals in the rock sample manifest as large particles composed of finer clay materials, intricately stacked, intertwined, and bonded with each other.

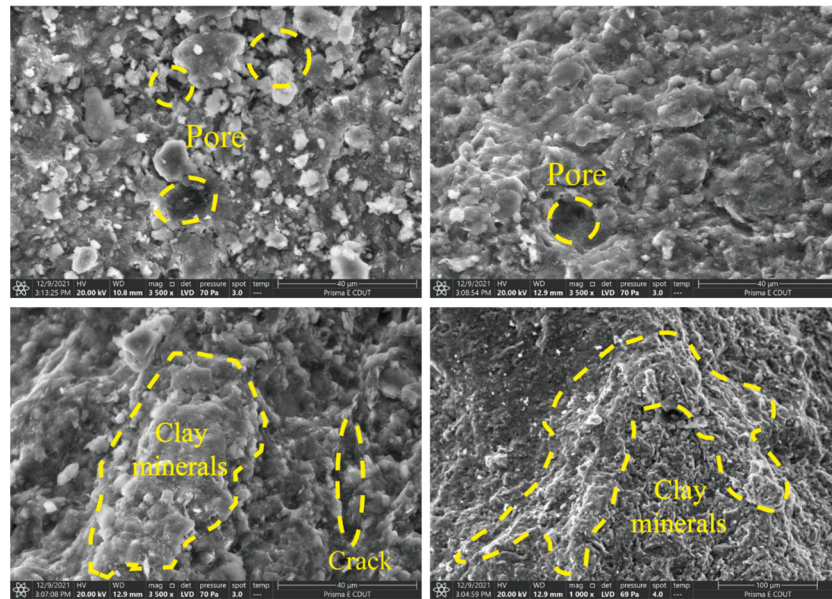


Figure 8. Typical SEM image of Neogene mudstone.

5. Discussion

The specimens in the experiments were derived from the Zhangjiawan landslide, with the surface layer being composed of loess and the lower part composed of fractured mudstone characterized by substantial porosity and susceptibility to softening and mudding. A weak sliding plane was formed once the water permeated the mudstone layer and led to rapid disintegration, softening, and mudding, as depicted in Figure 9. A slip zone can be found at approximately 14 m below the ground surface, where rock specimens S-13.7 and S-14.0 exhibit lower slake durability, signifying weaker abilities to resist softening and disintegration. Concurrently, S-13.7 and S-14.0, with a considerable plasticity index, are susceptible to plastic deformation.

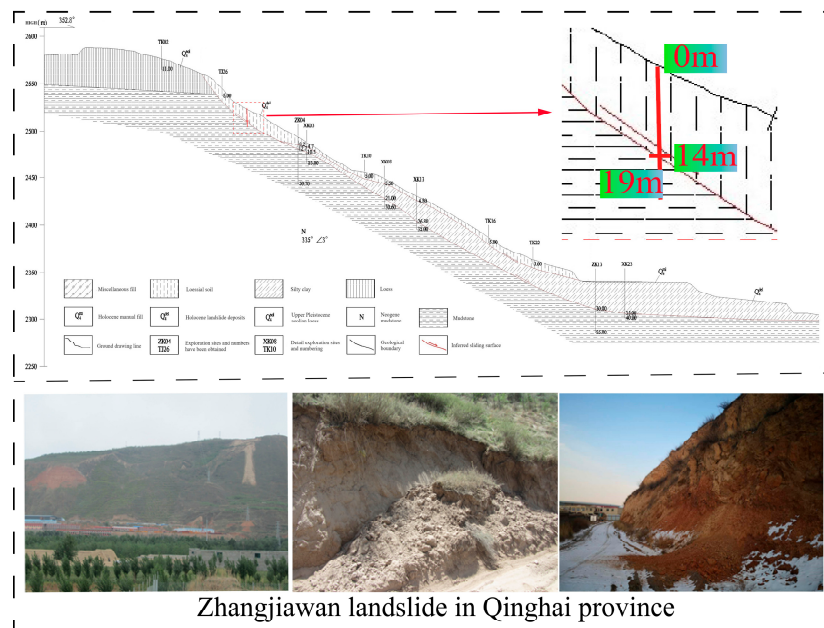


Figure 9. Longitudinal profile of the Zhangjiawan landslide and the sampling site.

In this case, mudstone in the slip zone exhibits instability, an aptitude for plastic deformation, and a tendency for disintegration. During the disintegration process, solid

particles detach from the rock mass, leading to a loosened pore structure and diminishing cohesion, further escalating landslide risks. The disintegration of mudstone results in a loss of structural cohesiveness and reduction in shear strength, leading to an unstable slope condition. Subsequent to disintegration, mudstone often exhibits a rising porosity, generating larger pores and microcracks that enhance soil permeability. Mudstone in slip zones shows strong susceptibility to hygroscopic swelling, prone to expansion deformation upon moisture interaction, compromising the slope stability. Water can further enlarge and intensify existing cracks, with the potential to induce stress readjustment within the rock mass. In addition, particle displacement might also change the permeation properties of rock materials, engendering latent slip surfaces and multiplying the risk of landslides. At the micro level, the primary pore structure consists of the pores and fractures formed between coarse particles, predominantly along particle edges and interstices, which give rise to the integrity of the mudstone. With the diminishment of cementation, micro pores and fractures become finer and interconnected, leading to a loose and discontinuous microstructure in the mudstone. In this case, particle misalignment occurs frequently, the entire microstructure presents as fragile and loose, and a detrital configuration emerges. The disassociation of the coarse particle framework within this loosened microstructure signals the impending instability of the overall structure.

6. Conclusions

Neogene mudstone characterized by distinctive mechanical behavior, widely existing in a red-layer area, plays a significant role in the stability and safety of geotechnical engineering. Investigating the disintegration characteristics of Neogene mudstone at various burial depths can contribute to providing theoretical support for the deformation properties of mudstone with underground engineering. This study investigated the effects of burial depth on the disintegration characteristics of Neogene mudstone through laboratory experiments and revealed the intrinsic links between the disintegration characteristics of mudstone and landslide disasters at the sampling site. Ignoring the influence of slip surfaces, increasing burial depth correlates with a gradual decline in the slake durability index, while the plasticity index manifests an upward trend. Greater depths can amplify the effects of groundwater and geo-stress on the mechanical behaviors of mudstone, heightening the risks associated with wetting and softening. In addition, groundwater activity may lead to mudstone dissolution, along with a reduction in cohesion and shear strength, potentially resulting in plastic or compressive deformation and further diminishing the disintegration of mudstone. The porosity, morphology, and connectivity of Neogene mudstone can be influenced via increasing the burial depth, and alterations in pore structure can decrease the permeability and consequently affect the disintegration characteristics and deformation of Neogene mudstone. It should be noted that the Neogene mudstone samples utilized in this study originated from a restricted area. The laboratory conditions may not fully replicate the natural scenarios where mudstones have been subjected to over-extensive geological epochs. Thus, the mudstone specimens used in further investigations should be captured from a more extensive array of geological contexts. The complex chemical, physical, and biological processes in natural conditions can be emulated utilizing techniques such as solution immersion or cyclic temperature and humidity trials.

Author Contributions: Conceptualization and writing—original draft, L.P.; investigation and methodology, W.D.; data curation and validation, G.B. and L.; visualization and writing—reviewing and editing, S.Y. and J.L.; supervision and project administration, P.F. All authors have read and agreed to the published version of the manuscript.

Funding: The authors are grateful for the Qinghai Province Central Government Guided Fund for Local Science and Technology Development Project (2021ZY014), Qinghai Province “Kunlun Talents” Top-Tier Talent Project for High-End Innovation and Entrepreneurship (2022-KY-34), and the Open Research Subject of Key Laboratory of Hydraulic and Waterway Engineering of the Ministry of Education, Chongqing Jiaotong University (SLK2023A02).

Data Availability Statement: The original contributions presented in the study are included in the article, further inquiries can be directed to the corresponding author.

Conflicts of Interest: The authors declare no conflicts of interest.

References

1. Liu, J.; Xu, Q.; Wang, S.; Siva Subramanian, S.; Wang, L.; Qi, X. Formation and chemo-mechanical characteristics of weak clay interlayers between alternative mudstone and sandstone sequence of gently inclined landslides in Nanjiang, SW China. *Bull. Eng. Geol. Environ.* **2020**, *79*, 4701–4715. [[CrossRef](#)]
2. Sadisun, I.A.; Bandonio; Shimada, H.; Ichinose, M.; Matsui, K. Physical disintegration characterization of mudrocks subjected to slaking exposure and immersion tests. *Indones. J. Geosci.* **2010**, *5*, 219–255. [[CrossRef](#)]
3. Wu, M.; Zhou, F.; Wang, J. Dem modeling of mini-triaxial test on soil-rock mixture considering particle shape effect. *Comput. Geotech.* **2023**, *153*, 105110. [[CrossRef](#)]
4. Mangano, G.; Alves, T.M.; Zecchin, M.; Civile, D.; Critelli, S. The Rossano-San Nicola Fault Zone evolution impacts the burial and maturation histories of the Crotona Basin, Calabrian Arc, Italy. *Pet. Geosci.* **2023**, *29*, 2022–2085. [[CrossRef](#)]
5. Mangano, G.; Ceramicola, S.; Alves, T.M.; Zecchin, M.; Civile, D.; Del Ben, A.; Critelli, S. A new large-scale gravitational complex discovered in the Squillace Embayment (central Mediterranean): Tectonic and geohazard implications. *Sci. Rep.* **2023**, *13*, 14695. [[CrossRef](#)] [[PubMed](#)]
6. Campilongo, G.; Campilongo, E.; Catanzariti, F.; Muto, F.; Ponte, M.; Critelli, S. Subsidence analysis by mean of DeGloT software: Application to the key-case of the Miocene-Quaternary Crotona Basin (Calabria, S. Italy). *Mar. Pet. Geol.* **2022**, *146*, 10596. [[CrossRef](#)]
7. Campilongo, G.; Ponte, M.; Muto, F.; Critelli, S.; Catanzariti, F.; Perri, F. Geotechnics, mineralogy and geochemistry of the Cutro Clay Formation, Calabria, Southern Italy. *J. Mediterr. Earth Sci.* **2022**, *14*, 11–26.
8. Li, H.; He, Y.; Xu, Q.; Deng, J.; Li, W.; Wei, Y.; Zhou, J. Sematic segmentation of loess landslides with STAPLE mask and fully connected conditional random field. *Landslides* **2023**, *20*, 367–380. [[CrossRef](#)]
9. Li, H.; He, Y.; Xu, Q.; Deng, J.; Li, W.; Wei, Y. Detection and segmentation of loess landslides via satellite images: A two-phase framework. *Landslides* **2022**, *19*, 673–686. [[CrossRef](#)]
10. Shi, J.S.; Wu, L.Z.; Qu, Y.X.; Li, B.; Wu, S.R. Neogene clay and its relation to landslides in the southwestern Loess Plateau, China. *Environ. Earth Sci.* **2018**, *77*, 1–11. [[CrossRef](#)]
11. Peng, J.; Leng, Y.; Zhu, X.; Wu, D.; Tong, X. Development of a loess-mudstone landslide in a fault fracture zone. *Environ. Earth Sci.* **2016**, *75*, 1–11. [[CrossRef](#)]
12. Kong, L.W.; Zeng, Z.X.; Bai, W.; Wang, M. Engineering geological properties of weathered swelling mudstones and their effects on the landslides occurrence in the Yanji section of the Jilin-Hunchun high-speed railway. *Bull. Eng. Geol. Environ.* **2018**, *77*, 1491–1503. [[CrossRef](#)]
13. Zhang, Z.; Liu, W.; Han, L.; Chen, X.; Cui, Q.; Yao, H.; Wang, Z. Disintegration behavior of strongly weathered purple mudstone in drawdown area of three gorges reservoir, China. *Geomorphology* **2018**, *315*, 68–79. [[CrossRef](#)]
14. Peng, J.; Tong, X.; Wang, S.; Ma, P. Three-dimensional geological structures and sliding factors and modes of loess landslides. *Environ. Earth Sci.* **2018**, *77*, 675. [[CrossRef](#)]
15. Conforti, M.; Muto, F.; Rago, V.; Critelli, S. Landslide inventory map of north-eastern Calabria (South Italy). *J. Maps* **2014**, *10*, 90–102. [[CrossRef](#)]
16. Zhang, Z.; Liu, W.; Cui, Q.; Han, L.; Yao, H. Disintegration characteristics of moderately weathered mudstone in drawdown area of Three Gorges Reservoir, China. *Arab. J. Geosci.* **2018**, *11*, 405–414. [[CrossRef](#)]
17. Su, X.; Tang, H.; Huang, L.; Shen, P.; Xia, D. The role of pH in red-stratum mudstone disintegration in the Three Gorges reservoir area, China, and the associated micromechanisms. *Eng. Geol.* **2020**, *279*, 105873. [[CrossRef](#)]
18. Feng, P.; Zhao, J.C.; Dai, F.; Wei, M.D.; Liu, B. Mechanical behaviors of conjugate-flawed rocks subjected to coupled static–dynamic compression. *Acta Geotech.* **2022**, *17*, 1765–1784. [[CrossRef](#)]
19. Feng, P.; Xu, Y.; Dai, F. Effects of dynamic strain rate on the energy dissipation and fragment characteristics of cross-fissured rocks. *Int. J. Rock Mech. Min. Sci.* **2021**, *138*, 104600. [[CrossRef](#)]
20. Luo, J.; Wu, Y.; Mi, D.; Ye, Q.; Huang, H.; Chang, Z.; Liu, X. Analysis of the distribution and microscopic characteristics and disintegration characteristics of carbonaceous rocks: A case study of the middle Devonian Luofu formation in western Guangxi of China. *Adv. Civ. Eng.* **2020**, *2020*, 8810648. [[CrossRef](#)]
21. Huang, K.; Kang, B.; Zha, F.; Li, Y.; Zhang, Q.; Chu, C. Disintegration characteristics and mechanism of red-bed argillaceous siltstone under drying–wetting cycle. *Environ. Earth Sci.* **2022**, *81*, 336. [[CrossRef](#)]
22. Gautam, T.P.; Shakoor, A. Comparing the slaking of clay-bearing rocks under laboratory conditions to slaking under natural climatic conditions. *Rock Mech. Rock Eng.* **2016**, *49*, 19–31. [[CrossRef](#)]
23. Fereidooni, D.; Khajevand, R. Utilization of the accelerated weathering test method for evaluating the durability of sedimentary rocks. *Bull. Eng. Geol. Environ.* **2019**, *78*, 2697–2716. [[CrossRef](#)]
24. Shen, P.; Tang, H.; Huang, L.; Wang, D. Experimental study of slaking properties of red-bed mudstones from the Three Gorges Reservoir area. *Mar. Georesources Geotechnol.* **2019**, *37*, 891–901. [[CrossRef](#)]

25. Sharma, B.; Bora, P.K. Plastic limit, liquid limit and undrained shear strength of soil—Reappraisal. *J. Geotech. Geoenviron. Eng.* **2003**, *129*, 774–777. [[CrossRef](#)]
26. Shakoor, A.; Gautam, T.P. Influence of geologic and index properties on disintegration behavior of clay-bearing rocks. *Environ. Eng. Geosci.* **2015**, *21*, 197–209. [[CrossRef](#)]
27. Shimobe, S.; Spagnoli, G. Relationships between undrained shear strength, liquidity index, and water content ratio of clays. *Bull. Eng. Geol. Environ.* **2020**, *79*, 4817–4828. [[CrossRef](#)]
28. Laguros, J.G. *Effect of Temperature on Some Engineering Properties of Clay Soils*; Highway Research Board: Washington, DC, USA, 1969; pp. 186–193.
29. Stanchi, S.D.; D’Amico, M.; Zanini, E.; Freppaz, M. Liquid and Plastic limits of mountain soils as a function of the soil and horizon type. *Catena* **2015**, *135*, 114–121. [[CrossRef](#)]
30. Jefferson, I.; Rogers, C.D.F. Liquid limit and the temperature sensitivity of clays. *Eng. Geol.* **1998**, *49*, 95–109. [[CrossRef](#)]
31. El Swaify, S.A.; Ahmed, S.; Swindale, L.D. Effects of adsorbed cations on physical properties of tropical red and tropical black earths: II. Liquid limit, degree of dispersion, and moisture retention. *J. Soil Sci.* **1970**, *21*, 188–198. [[CrossRef](#)]
32. Davidson, D.A. Problems in the determination of plastic and liquid limits of remoulded soils using a drop-cone penetrometer. *Earth Surf. Process. Landf.* **1983**, *8*, 171–175. [[CrossRef](#)]
33. Stanchi, S.; Catoni, M.; D’Amico, M.E.; Falsone, G.; Bonifacio, E. Liquid and plastic limits of clayey, organic C-rich mountain soils: Role of organic matter and mineralogy. *Catena* **2017**, *151*, 238–246. [[CrossRef](#)]
34. Tang, H.D.; Zhu, M.L. Timely spread characteristics of micro- and meso-scale fractures based on SEM experiment. *Environ. Earth Sci.* **2020**, *79*, 1–20. [[CrossRef](#)]
35. Howarth, D.F.; Rowlands, J.C. Quantitative assessment of rock texture and correlation with drillability and strength properties. *Rock Mech. Rock Eng.* **1987**, *20*, 57–85. [[CrossRef](#)]
36. Campbell, D.H.; Galehouse, J.S. Quantitative clinker microscopy with the light microscope. *Cem. Concr. Aggreg.* **1991**, *13*, 94–96.
37. Zhou, M.; Li, J.; Luo, Z.; Sun, J.; Xu, F.; Jiang, Q.; Deng, H. Impact of water-rock interaction on the pore structures of red-bed soft rock. *Sci. Rep.* **2021**, *11*, 7398. [[CrossRef](#)]
38. Xiaoshuai, X.; Huasong, C.; Xinhong, X.; Jing, W.; Jiawen, Z. Micro-structural characteristics and softening mechanism of red-bed soft rock under water-rock interaction condition. *J. Eng. Geol.* **2019**, *27*, 966–972.
39. Li, A.; Deng, H.; Wang, X.; Luo, J.; Zhang, J. Research on creep characteristics and constitutive model of red bed mudstone under saturated-dehydrated cycle. *J. Eng. Geol.* **2021**, *29*, 843–850.
40. Dhakal, G.; Yoneda, T.; Kato, M.; Kaneko, K. Slake durability and mineralogical properties of some pyroclastic and sedimentary rocks. *Eng. Geol.* **2002**, *65*, 31–45. [[CrossRef](#)]
41. Zhang, S.; Xu, Q.; Hu, Z. Effects of rainwater softening on red mudstone of deep-seated landslide, Southwest China. *Eng. Geol.* **2016**, *204*, 1–13. [[CrossRef](#)]
42. Wu, M.; Wang, J. Exploring particle breakage in sand under triaxial shearing using combined X-ray tomography and particle tracking method. *Géotechnique* **2023**, 1–40. [[CrossRef](#)]
43. Franklin, J.A.; Chandra, R. The slake-durability test. *Int. J. Rock Mech. Min. Sci. Geomech. Abstr.* **1972**, *9*, 325–328. [[CrossRef](#)]
44. Ulusay, R. *The ISRM Suggested Methods for Rock Characterization, Testing and Monitoring: 2007–2014*; Springer International Publishing: Berlin/Heidelberg, Germany, 2014; Volume 15, pp. 47–48.
45. Ahmad, A.; Lopulisa, C.; Baja, S.; Imran, A.M. The correlation of soil liquid limit and plasticity index for predicting soil susceptibility: A case study on landslides area in South Sulawesi. *IOP Conf. Ser. Earth Environ. Sci.* **2019**, *235*, 012007. [[CrossRef](#)]
46. Bhattarai, P.; Marui, H.; Tiwari, B.; Watanabe, N.; Tuladhar, G.R. Depth-wise variation of physical and mechanical properties of mudstone in relation to weathering. *J. Jpn. Landslide Soc.* **2007**, *44*, 79–89. [[CrossRef](#)]
47. Hanke, R.; Fuchs, T.; Salamon, M.; Zabler, S. X-ray microtomography for materials characterization. In *Materials Characterization Using Nondestructive Evaluation (NDE) Methods*; Woodhead Publishing: Cambridge, UK, 2016; pp. 45–79.
48. Zhou, W.; Apkarian, R.; Wang, Z.L.; Joy, D. Fundamentals of scanning electron microscopy (SEM). In *Scanning Microscopy for Nanotechnology*; Springer: New York, NY, USA, 2007; pp. 1–40. [[CrossRef](#)]

Disclaimer/Publisher’s Note: The statements, opinions and data contained in all publications are solely those of the individual author(s) and contributor(s) and not of MDPI and/or the editor(s). MDPI and/or the editor(s) disclaim responsibility for any injury to people or property resulting from any ideas, methods, instructions or products referred to in the content.